DØ Note 6111-CONF

Precise study of the Z/γ^* boson transverse momentum distribution in $p\bar{p}$ collisions using a novel technique

The DØ Collaboration
URL http://www-d0.fnal.gov
(Dated: August 24, 2010)

Using 7.3 fb^{-1} of $p\bar{p}$ collisions collected by the D0 detector at the Fermilab Tevatron, we study the transverse momentum distribution of Z/γ^* bosons. Within a dilepton invariant mass window of 70–110 GeV, 455k dielectron events and 511k dimuon events are selected. In bins of boson rapidity, the normalised differential cross section is measured as a function of the variable ϕ^*_η, which is sensitive to the same physics as the transverse momentum distribution, but less susceptible to the effects of detector resolution and efficiency. We find that QCD predictions from the Monte Carlo program ResBos are unable to describe the detailed shape of the data corrected for detector effects. In particular, a prediction that includes the effect of small-x broadening is very strongly disfavoured.

Preliminary Results for Summer 2010 Conferences

Due to the colourless and low background final state, Z/γ^* boson decays into electron and muon pairs provide an excellent testing ground for QCD predictions at hadron colliders. Resummation techniques [1] allow calculation of the distribution of Z/γ^* boson transverse momentum, p_T, within the framework of perturbative QCD, even at relatively low p_T (e.g., $p_T < 30$ GeV). However, additional non-perturbative form factors must be determined in global fits to experimental data [2]. A dependence of these non-perturbative form factors on parton momentum fraction, x, was introduced [3] in order to improve the description of data on hadron production in deep inelastic electron-proton scattering at HERA. Such "small-x broadening" would have a notable effect on the vector boson p_T distribution expected at the LHC [4] and, thus, influence the measurement of the W boson mass as well as searches for Higgs bosons and new physics at the LHC. It is important to study quantitatively such effects at the Tevatron, where they can be probed using the dependence of the p_T distribution on boson rapidity:

$$y = \frac{1}{2}\ln\left(\frac{E - p_z}{E + p_z}\right),$$

where E is the energy of the boson and p_z is the component of its momentum parallel to the beam axis.

In the region of low Z/γ^* boson p_T, the precision of the most recent measurements at the Tevatron [5, 6] was dominated by uncertainties in correcting for detector resolution and efficiency. Furthermore, the choice of bin widths was restricted by experimental resolution rather than event statistics. The variable a_T, which corresponds to the component of p_T that is transverse to the dilepton thrust axis, has been proposed as an alternative analysing variable that is sensitive to the same physics as the p_T, but less susceptible to the detector effects [7]. The a_T distribution was subsequently calculated to next-to-leading-log (NLL) accuracy using resummation techniques [8]. Additional analysing variables with even better experimental resolution have recently been proposed and studied [9]. The optimal variable was found to be ϕ^*_η, which is defined as:

$$\phi^*_\eta = \tan\left(\frac{\phi_{\rm acop}}{2}\right)\sin(\theta^*_\eta),$$

where $\phi_{\rm acop}$ is the acoplanarity angle, given by:

$$\phi_{\rm acop} = \pi - \Delta\phi_{\ell\ell},$$

and $\Delta\phi_{\ell\ell}$ is the difference in azimuthal angle, ϕ, between the two lepton candidates. The variable θ^*_η is a measure of the scattering angle of the leptons with respect to the beam direction in the rest frame of the dilepton system. It is defined [9] by:

$$\cos(\theta^*_\eta) = \tanh\left(\frac{\eta^- - \eta^+}{2}\right),$$

where η^- and η^+ are the pseudorapidities of the negatively and positively charged lepton, respectively, $\eta = -\ln[\tan(\theta/2)]$ and θ is the angle with respect to the beam direction in the laboratory frame. Because $\phi_{\rm acop}$ and θ^*_η depend exclusively on the directions of the two leptons, ϕ^*_η is experimentally very well measured compared to any quantities that rely on the momenta of the leptons.

This Letter describes a measurement of the normalised ϕ^*_η distribution, $(1/\sigma)\times(d\sigma/d\phi^*_\eta)$, in bins of $|y|$, using 7.3 fb^{-1} of $p\bar{p}$ collisions collected by the D0 detector at the Fermilab Tevatron. The ϕ^*_η distributions are measured in both dielectron and dimuon events and are corrected for detector resolution and efficiency. We correct back to the level of observable particles, with particle level kinematic selection criteria that match those applied in the selection of candidate events in the data [10]. Particle level electrons are defined as the four-vector sum of any electrons and photons within a cone of $\Delta\mathcal{R} = \sqrt{(\Delta\eta)^2 + (\Delta\phi)^2} < 0.2$ around a seed electron, where $\Delta\eta$ ($\Delta\phi$) is the distance in η (ϕ) from the seed electron; this attempts to mimic the measurement of electron energy in a calorimeter. Particle level muons are defined after any QED final state radiation; this attempts to mimic the measurement of muon momentum in a tracking detector. The kinematic selection criteria are: candidate electrons must satisfy $|\eta| < 3$ and $p_T > 20$ GeV; candidate muons must satisfy $|\eta| < 2$ and $p_T > 15$ GeV; the dilepton invariant mass must fall within the range 70–110 GeV.

The corrected data are compared to predictions from the Monte Carlo (MC) program ResBos [11] with the above mentioned kinematic selection criteria applied at the particle level. ResBos generates Z/γ^* boson events with initial state QCD corrections to next-to-leading order (NLO) and NLL accuracy together with: a non-perturbative form factor [2], whose width in high energy hadron-hadron collisions is controlled primarily by the parameter g_2 (with default value 0.68 GeV^2); an additional next-to-NLO (NNLO) K-factor [12]; CTEQ6.6 NLO PDFs [13]; and QED radiative corrections from photos [14].

The D0 detector [15] consists of: silicon microstrip (SMT) and central fiber (CFT) tracking detectors, located within a 2 T superconducting solenoid; a liquid-argon/uranium sampling calorimeter; and an outer muon system consisting of tracking and scintillation detectors located before and after 1.8 T toroids. Candidate dielectron events are required to satisfy a trigger based on the identification of a single electron and to contain two clusters reconstructed in the calorimeter with a transverse and longitudinal shower profile loosely consistent with that expected of an electron. Candidate dimuon events are required to satisfy a trigger based on the identification of a single muon and to contain two muons reconstructed either in the outer muon system, or as an energy deposit consistent with the passage of a minimum-ionizing particle in the calorimeter. In order to ensure an accurate measurement of the lepton directions at the point of production, the two leptons are required to be matched to a pair of oppositely charged particle tracks reconstructed in the central tracking detectors. Candidate leptons resulting from misidentified hadrons or produced by the decay of hadrons are suppressed by requiring that they be isolated from other particles in the event and, in the case of electrons with $|\eta| < 1.1$, by requiring consistency of the energy measured in the calorimeter with the momentum measured in the central tracking detectors. Contamination from cosmic ray muons is eliminated by a requirement that the muons originate from the $p\bar{p}$ collision point and by rejecting events in which the two muon candidates are back to back in η.

The corrections to the observed ϕ^*_η distribution for detector resolution and efficiency are evaluated using Z/γ^* boson MC events that are generated with PYTHIA [16] and passed through a GEANT-based [17] simulation of the detector. These fully simulated MC events are re-weighted at the generator level in two dimensions (p_T^Z and $|y|$) to match the predictions of RESBOS. In addition, adjustments are made to improve the accuracy of the following aspects of the detector simulation: electron energy and muon p_T scale and resolution; track ϕ and η resolutions; trigger efficiencies; and relevant offline reconstruction and selection efficiencies. Variations in the above adjustments to the underlying physics and the detector simulation are included in the assessment of the systematic uncertainties on the correction factors.

The systematic uncertainties due to electron energy and muon p_T scale and resolution are very small, and arise only due to the kinematic requirements in the event selection. The measured ϕ^*_η distribution is, however, susceptible to modulations in ϕ of the lepton identification and trigger efficiencies, which result, e.g., from detector module boundaries in the calorimeter and muon systems. Particular care has been taken (a) in the choice of lepton identification criteria in order to minimize such modulations and (b) to ensure that such modulations are well simulated in the MC. For example, the requirements imposed on shower profile are much looser than those usually employed in electron identification within D0, because tight requirements are particularly inefficient in the regions close to module boundaries in the calorimeter. Similarly, the inclusion of muon candidates identified in the calorimeter reduces the effect of gaps between modules in the outer muon system.

The background processes, $Z \to \tau^-\tau^+$ and $W \to l\nu$ (+jets), are also simulated using MC events generated with PYTHIA. The background from multijet events is estimated directly from data. The fraction of background events is 0.1% for the dielectron channel, and 0.2% for the dimuon channel.

Since the experimental resolution in ϕ^*_η is very good, the fractions of accepted events that fall within the same bin in ϕ^*_η at the particle level and reconstructed detector level in the MC are high, having typical (lowest) values of around 98% (92%). Therefore, simple bin-by-bin corrections of the ϕ^*_η distribution are sufficient. In almost all ϕ^*_η bins the total systematic uncertainty is substantially smaller than the statistical uncertainty.

Figure 1 shows the corrected ϕ^*_η distributions together with predictions from RESBOS. Figure 2 shows the ratio of the corrected ϕ^*_η distributions to the RESBOS predictions in both the dielectron and dimuon data. The yellow band represents the uncertainty in the RESBOS prediction due to PDFs, which is evaluated using the CTEQ6.6 NLO error PDFs [13]. Since the particle level definitions for electrons and muons to which the data are corrected are slightly different, Fig. 2 represents the most appropriate way to make a consistency check between the dielectron and dimuon data.

The general shape of the ϕ^*_η distribution is broadly described by RESBOS. However, the small statistical uncertainties resulting from the large dilepton data sets, combined with the fine binning and small systematic uncertainties resulting from the use of ϕ^*_η as the analysing variable, expose the failure of RESBOS to describe the data in detail. The corrected dielectron and dimuon data are consistent with one another. Given that the experimental acceptance corrections are very different in the two channels, this represents a powerful cross check of the corrected distributions.

In order to allow RESBOS the best possible chance to describe the data, the g_2 parameter is allowed to float. Table I shows the values of g_2 that best describe the corrected data, in each $|y|$ bin and channel. It can be seen that the fitted values of g_2 show a monotonic decrease with increasing $|y|$ for both dielectron and dimuon data. That is, the width of the ϕ^*_η distribution becomes narrower with increasing $|y|$ faster in the data than is predicted by RESBOS with default parameters. This is the opposite of the behaviour expected from the small-x broadening hypothesis [3, 4]. Figures 1 and 2 confirm that the prediction from RESBOS with small-x broadening is in very poor agreement with data. It can also be seen that choosing the closest available g_2 value (0.64 GeV^2) to that which best describes the data over all ranges of $|y|$ has very little effect on the level of agreement with data.

Channel	$\lvert y\rvert < 1$	$1 \leq \lvert y\rvert < 2$	$\lvert y\rvert \geq 2$
ee	0.646 ± 0.012	0.590 ± 0.016	0.495 ± 0.047
$\mu\mu$	0.661 ± 0.011	0.628 ± 0.019	–

TABLE I: Value of g_2 (GeV^2) that best describes the corrected data in each $|y|$ bin and channel.

In summary, using 7.3 fb^{-1} of $p\bar{p}$ collisions collected by the D0 detector at the Fermilab Tevatron, we study with unprecedented precision the p_T distribution of Z/γ^* bosons in dielectron and dimuon final states. In bins of boson rapidity, the normalised differential cross section is measured as a function of the variable ϕ^*_η, which is sensitive to the same physics as the p_T distribution, but less susceptible to detector resolution and efficiency effects. Predictions from ResBos are unable to describe the detailed shape of the corrected data, and a prediction that includes the effect of small-x broadening is very strongly disfavoured.

Tabulated values of the corrected $(1/\sigma) \times (d\sigma/d\phi^*_\eta)$ distributions for each $|y|$ bin and channel are provided [18].

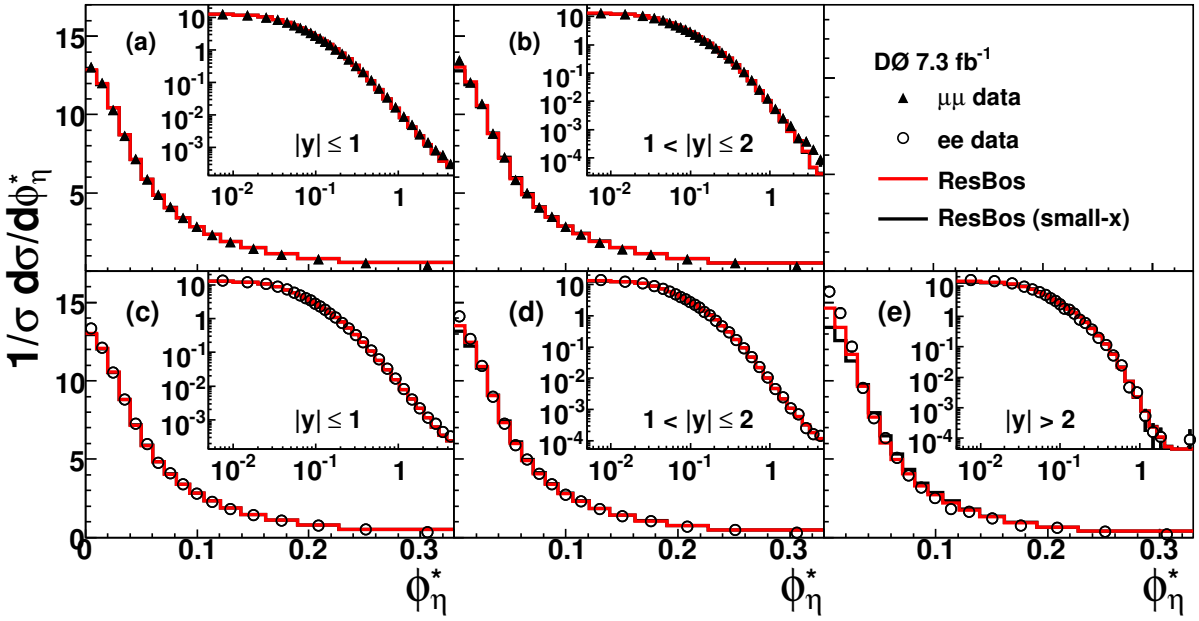

FIG. 1: (color online) Comparison of the corrected distribution of $(1/\sigma) \times (d\sigma/d\phi^*_\eta)$ with predictions from ResBos for dimuon events with (a) $|y| < 1$ and (b) $1 \leq |y| < 2$; and dielectron events with (c) $|y| < 1$, (d) $1 \leq |y| < 2$ and (e) $|y| \geq 2$. The larger plots show the distribution with linear scales over the restricted range $0 < \phi^*_\eta < 0.3$ and the insets show the distribution with log scales over the full range of ϕ^*_η. The error bars on the data points represent statistical and systematic uncertainties combined in quadrature. The predictions from default ResBos are shown as the red histogram and from ResBos with small-x broadening as the black histogram.

We thank the staffs at Fermilab and collaborating institutions, and acknowledge support from the DOE and NSF (USA); CEA and CNRS/IN2P3 (France); FASI, Rosatom and RFBR (Russia); CNPq, FAPERJ, FAPESP and FUNDUNESP (Brazil); DAE and DST (India); Colciencias (Colombia); CONACyT (Mexico); KRF and KOSEF (Korea); CONICET and UBACyT (Argentina); FOM (The Netherlands); STFC and the Royal Society (United Kingdom); MSMT and GACR (Czech Republic); CRC Program and NSERC (Canada); BMBF and DFG (Germany); SFI (Ireland); The Swedish Research Council (Sweden); and CAS and CNSF (China).

[1] J. Collins, D. Soper, G. Sterman, Nucl. Phys. B **250**, 199 (1985).
[2] F. Landry *et al.*, Phys. Rev. D **67**, 073016 (2003).
[3] P. Nadolsky, D.R.Stump, C.P. Yuan, Phys. Rev. D **64**, 114011 (2001).
[4] S. Berge, P. Nadolsky, F. Olness, C.P. Yuan, Phys. Rev. D **72**, 033015 (2005).
[5] D0 Collaboration, V. M. Abazov *et al.*, Phys. Rev. Lett. **100**, 102002 (2008).

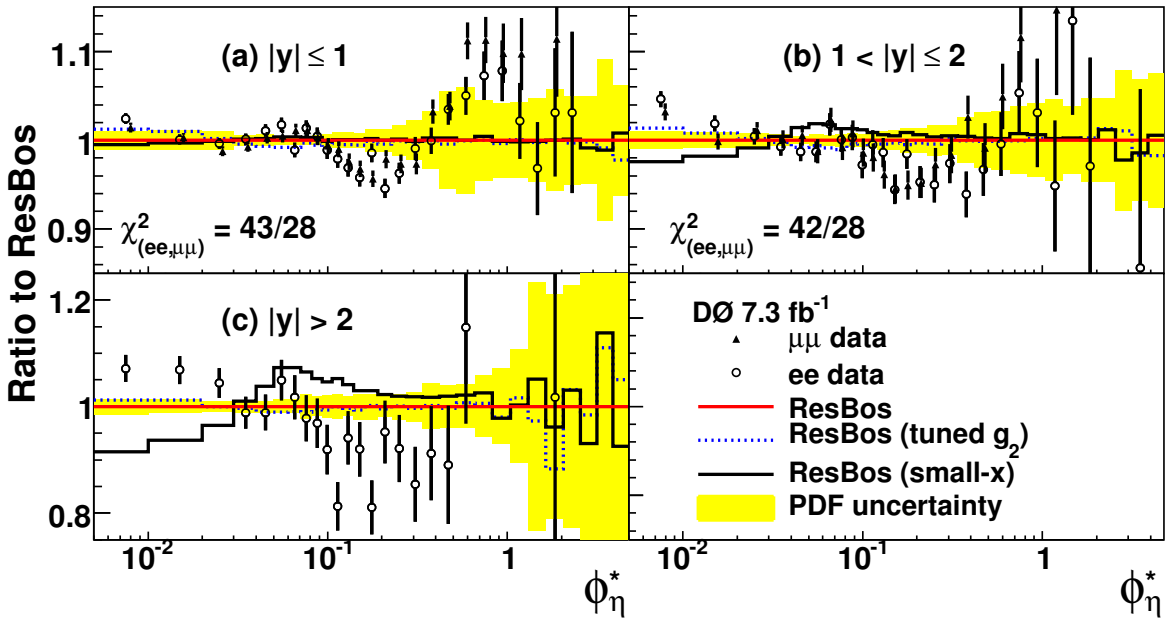

FIG. 2: (color online) Ratio of the corrected distribution of $(1/\sigma) \times (d\sigma/d\phi^*_\eta)$ in dielectron and dimuon data to predictions from ResBos with default settings for: (a) $|y| < 1$, (b) $1 \leq |y| < 2$ and (c) $|y| \geq 2$. The error bars on the data points represent statistical and systematic uncertainties combined in quadrature. In (a) and (b) a χ^2 for the comparison of the dielectron and dimuon data, $\chi^2_{ee/\mu\mu}$, is calculated assuming uncorrelated uncertainties. The yellow band around the ResBos prediction represents the uncertainty due to PDFs. Also shown are the changes to the ResBos predictions when (dotted blue histogram) the value of g_2 is adjusted from its default value to that which best describe the corrected data, and when (solid black histogram) the small-x broadening option is enabled. *N.B. this figure does need some work on presentation.*

[6] D0 Collaboration, V. M. Abazov *et al.*, arXiv:1006.0618 [hep-ex] *submitted to Phys. Lett. B* (2010).
[7] M. Vesterinen, T. R. Wyatt, Nucl. Instrum. Methods Phys. Res. A **602**, 432 (2009).
[8] A. Banfi, M. Dasgupta, R. Delgado, JHEP 0912:022 (2009).
[9] A. Banfi, S. Redford, M. Vesterinen, P. Waller, T. R. Wyatt, arXiv:XXXXX [hep-ph] (2010) *in preparation.*
[10] We follow the recommendations of, J. M. Butterworth *et al.*, *The Tools and Monte Carlo Working Group Summary Report from the Les Houches 2009 Workshop on TeV Colliders*, arXiv:1003.1643 [hep-ph] (2010).
[11] C. Balazs, C.P. Yuan, Phys. Rev. D **56**, 5558 (1997).
[12] P. B. Arnold, M. H.Reno, Nucl. Phys. B **319**, 37 (1989); B **330**, 284(E) (1990).
[13] P. Nadolsky *et al.*, hep-ph/0802.0007 (2008).
[14] E. Barberio and Z. Was, Comput. Phys. Commun. **79**, 291 (1994).
[15] D0 Collaboration, V. M. Abazov *et al.*, Nucl. Instrum. Methods Phys. Res. A **565**, 463 (2006).
[16] T. Sjöstrand *et al.*, Comp. Phys. Comm. **135**, 238 (2001).
[17] S. Agostinelli *et al.*., Nucl. Instrum. Methods Phys. Res. A **506**, 250 (2003).
[18] See the supplementary material at (URL NEEDED).

Supplementary Material

Tables II–VI show the values of the corrected $(1/\sigma) \times (d\sigma/d\phi^*_\eta)$ distributions for each $|y|$ bin and channel. The first uncertainty is statistical and the second systematic.

TABLE II: The corrected $(1/\sigma) \times (d\sigma/d\phi^*_\eta)$ distribution for the dielectron channel and $|y| \leq 1$.

bin	range	$(1/\sigma) \times (d\sigma/d\phi^*_\eta)$
1	0.000-0.010	13.283 ± 0.066 ± 0.019
2	0.010-0.020	12.040 ± 0.062 ± 0.013
3	0.020-0.030	10.466 ± 0.058 ± 0.012
4	0.030-0.040	8.761 ± 0.053 ± 0.009
5	0.040-0.050	7.214 ± 0.048 ± 0.006
6	0.050-0.060	5.933 ± 0.044 ± 0.005
7	0.060-0.071	4.749 ± 0.038 ± 0.005
8	0.071-0.081	4.070 ± 0.035 ± 0.003
9	0.081-0.093	3.392 ± 0.031 ± 0.005
10	0.093-0.106	2.794 ± 0.026 ± 0.003
11	0.106-0.121	2.271 ± 0.022 ± 0.005
12	0.121-0.139	1.819 ± 0.018 ± 0.003
13	0.139-0.162	1.406 ± 0.014 ± 0.003
14	0.162-0.190	1.078 ± 0.011 ± 0.002
15	0.190-0.227	0.740 ± 0.008 ± 0.001
16	0.227-0.275	0.510 ± 0.006 ± 0.001
17	0.275-0.337	0.329 ± 0.004 ± 0.001
18	0.337-0.418	0.195 ± 0.003 ± 0.000
19	0.418-0.523	0.114 ± 0.002 ± 0.000
bin	range	$(1/\sigma) \times (d\sigma/d\phi^*_\eta)$ $(\times 1000)$
20	0.523-0.657	61.037 ± 1.210 ± 0.120
21	0.657-0.827	32.354 ± 0.794 ± 0.084
22	0.827-1.041	16.437 ± 0.502 ± 0.092
23	1.041-1.309	8.087 ± 0.325 ± 0.064
24	1.309-1.640	3.948 ± 0.205 ± 0.041
25	1.640-2.049	2.222 ± 0.146 ± 0.046
26	2.049-2.547	1.171 ± 0.097 ± 0.029
27	2.547-3.151	0.761 ± 0.072 ± 0.025
28	3.151-3.878	0.429 ± 0.049 ± 0.013
29	3.878-4.749	0.319 ± 0.040 ± 0.013

TABLE III: The corrected $(1/\sigma) \times (d\sigma/d\phi^*_\eta)$ distribution for the dielectron channel and $1 \leq |y| \leq 2$.

bin	range	$(1/\sigma) \times (d\sigma/d\phi^*_\eta)$
1	0.000-0.010	14.069 ± 0.103 ± 0.052
2	0.010-0.020	12.630 ± 0.098 ± 0.045
3	0.020-0.030	10.917 ± 0.091 ± 0.030
4	0.030-0.040	8.944 ± 0.082 ± 0.021
5	0.040-0.050	7.223 ± 0.074 ± 0.010
6	0.050-0.060	5.886 ± 0.066 ± 0.008
7	0.060-0.071	4.969 ± 0.060 ± 0.004
8	0.071-0.081	4.050 ± 0.053 ± 0.007
9	0.081-0.093	3.382 ± 0.047 ± 0.005
10	0.093-0.106	2.718 ± 0.040 ± 0.008
11	0.106-0.121	2.291 ± 0.034 ± 0.010
12	0.121-0.139	1.814 ± 0.028 ± 0.009
13	0.139-0.162	1.346 ± 0.021 ± 0.008
14	0.162-0.190	1.037 ± 0.017 ± 0.005
15	0.190-0.227	0.706 ± 0.012 ± 0.005
16	0.227-0.275	0.462 ± 0.009 ± 0.004
17	0.275-0.337	0.293 ± 0.006 ± 0.003
18	0.337-0.418	0.164 ± 0.004 ± 0.002
19	0.418-0.523	0.092 ± 0.003 ± 0.001
bin	range	$(1/\sigma) \times (d\sigma/d\phi^*_\eta)$ $(\times 1000)$
20	0.523-0.657	46.427 ± 1.608 ± 0.354
21	0.657-0.827	22.924 ± 1.009 ± 0.104
22	0.827-1.041	10.319 ± 0.596 ± 0.094
23	1.041-1.309	4.433 ± 0.336 ± 0.053
24	1.309-1.640	2.451 ± 0.224 ± 0.035
25	1.640-2.049	1.070 ± 0.129 ± 0.033
26	2.049-2.547	0.697 ± 0.091 ± 0.029
27	2.547-3.151	0.253 ± 0.048 ± 0.013
28	3.151-3.878	0.157 ± 0.035 ± 0.006
29	3.878-4.749	0.142 ± 0.032 ± 0.009

TABLE IV: The corrected $(1/\sigma) \times (d\sigma/d\phi^*_\eta)$ distribution for the dielectron channel and $|y| > 2$.

bin	range	$(1/\sigma) \times (d\sigma/d\phi^*_\eta)$
1	0.000-0.010	15.665 ± 0.362 ± 0.028
2	0.010-0.020	14.292 ± 0.344 ± 0.031
3	0.020-0.030	12.164 ± 0.320 ± 0.030
4	0.030-0.040	9.512 ± 0.281 ± 0.029
5	0.040-0.050	7.588 ± 0.250 ± 0.010
6	0.050-0.060	6.328 ± 0.227 ± 0.016
7	0.060-0.071	5.059 ± 0.203 ± 0.012
8	0.071-0.081	3.966 ± 0.174 ± 0.005
9	0.081-0.093	3.185 ± 0.151 ± 0.006
10	0.093-0.106	2.517 ± 0.126 ± 0.009
11	0.106-0.121	1.795 ± 0.099 ± 0.008
12	0.121-0.139	1.647 ± 0.086 ± 0.005
13	0.139-0.162	1.219 ± 0.067 ± 0.002
14	0.162-0.190	0.764 ± 0.047 ± 0.005
15	0.190-0.227	0.608 ± 0.037 ± 0.003
16	0.227-0.275	0.370 ± 0.025 ± 0.003
17	0.275-0.337	0.196 ± 0.016 ± 0.002
18	0.337-0.418	0.112 ± 0.011 ± 0.001
19	0.418-0.523	0.051 ± 0.006 ± 0.001
bin	range	$(1/\sigma) \times (d\sigma/d\phi^*_\eta)$ $(\times 1000)$
20	0.523-0.657	24.365 ± 3.764 ± 0.630
21	0.657-0.827	4.667 ± 1.568 ± 0.110
22	0.827-1.041	3.198 ± 1.209 ± 0.156
23	1.041-1.309	0.539 ± 0.381 ± 0.021
24	1.309-1.640	0.158 ± 0.158 ± 0.009
25	1.640-2.049	0.112 ± 0.112 ± 0.008

TABLE V: The corrected $(1/\sigma) \times (d\sigma/d\phi^*_\eta)$ distribution for the dimuon channel and $|y| \leq 1$.

bin	range	$(1/\sigma) \times (d\sigma/d\phi^*_\eta)$
1	0.000-0.010	12.969 ± 0.058 ± 0.027
2	0.010-0.020	11.944 ± 0.055 ± 0.018
3	0.020-0.030	10.237 ± 0.051 ± 0.013
4	0.030-0.040	8.604 ± 0.047 ± 0.009
5	0.040-0.050	7.111 ± 0.043 ± 0.013
6	0.050-0.060	5.852 ± 0.038 ± 0.009
7	0.060-0.071	4.864 ± 0.035 ± 0.010
8	0.071-0.081	4.078 ± 0.031 ± 0.005
9	0.081-0.093	3.396 ± 0.027 ± 0.005
10	0.093-0.106	2.828 ± 0.024 ± 0.004
11	0.106-0.121	2.320 ± 0.020 ± 0.003
12	0.121-0.139	1.851 ± 0.016 ± 0.003
13	0.139-0.162	1.439 ± 0.013 ± 0.003
14	0.162-0.190	1.063 ± 0.010 ± 0.002
15	0.190-0.227	0.782 ± 0.007 ± 0.002
16	0.227-0.275	0.527 ± 0.005 ± 0.001
17	0.275-0.337	0.332 ± 0.004 ± 0.001
18	0.337-0.418	0.209 ± 0.003 ± 0.001
19	0.418-0.523	0.118 ± 0.002 ± 0.000
bin	range	$(1/\sigma) \times (d\sigma/d\phi^*_\eta)$ $(\times 1000)$
20	0.523-0.657	66.803 ± 1.156 ± 0.339
21	0.657-0.827	34.940 ± 0.749 ± 0.279
22	0.827-1.041	17.380 ± 0.477 ± 0.199
23	1.041-1.309	8.995 ± 0.313 ± 0.084
24	1.309-1.640	4.899 ± 0.213 ± 0.054
25	1.640-2.049	2.546 ± 0.137 ± 0.053
26	2.049-2.547	1.411 ± 0.094 ± 0.036
27	2.547-3.151	0.824 ± 0.065 ± 0.019
28	3.151-3.878	0.570 ± 0.051 ± 0.016
29	3.878-4.749	0.311 ± 0.035 ± 0.010

TABLE VI: The corrected $(1/\sigma) \times (d\sigma/d\phi^*_\eta)$ distribution for the dimuon channel and $1 \leq |y| \leq 2$.

bin	range	$(1/\sigma) \times (d\sigma/d\phi^*_\eta)$
1	0.000-0.010	13.381 ± 0.105 ± 0.049
2	0.010-0.020	11.998 ± 0.100 ± 0.026
3	0.020-0.030	10.638 ± 0.094 ± 0.015
4	0.030-0.040	8.751 ± 0.086 ± 0.014
5	0.040-0.050	7.225 ± 0.077 ± 0.014
6	0.050-0.060	5.803 ± 0.069 ± 0.030
7	0.060-0.071	4.973 ± 0.063 ± 0.010
8	0.071-0.081	4.040 ± 0.056 ± 0.006
9	0.081-0.093	3.446 ± 0.050 ± 0.010
10	0.093-0.106	2.816 ± 0.043 ± 0.007
11	0.106-0.121	2.327 ± 0.036 ± 0.007
12	0.121-0.139	1.828 ± 0.029 ± 0.004
13	0.139-0.162	1.413 ± 0.023 ± 0.002
14	0.162-0.190	1.064 ± 0.018 ± 0.003
15	0.190-0.227	0.757 ± 0.013 ± 0.002
16	0.227-0.275	0.516 ± 0.009 ± 0.002
17	0.275-0.337	0.328 ± 0.007 ± 0.001
18	0.337-0.418	0.200 ± 0.005 ± 0.001
19	0.418-0.523	0.107 ± 0.003 ± 0.001
bin	range	$(1/\sigma) \times (d\sigma/d\phi^*_\eta)$ $(\times 1000)$
20	0.523-0.657	55.041 ± 1.867 ± 0.140
21	0.657-0.827	26.403 ± 1.160 ± 0.228
22	0.827-1.041	12.414 ± 0.726 ± 0.162
23	1.041-1.309	5.303 ± 0.434 ± 0.065
24	1.309-1.640	2.549 ± 0.276 ± 0.047
25	1.640-2.049	1.322 ± 0.209 ± 0.060
26	2.049-2.547	0.514 ± 0.116 ± 0.034
27	2.547-3.151	0.388 ± 0.097 ± 0.037
28	3.151-3.878	0.194 ± 0.059 ± 0.020
29	3.878-4.749	0.087 ± 0.039 ± 0.003